

# Cobalt-based Nanoreactors in Combined Fischer-Tropsch Synthesis and Hydroprocessing: Effects on Methane and CO<sub>2</sub> Selectivity

Angela Straß-Eifert,<sup>[a]</sup> Thomas L. Sheppard,<sup>[b, c]</sup> Henning Becker,<sup>[a]</sup> Jens Friedland,<sup>[a]</sup> Anna Zimina,<sup>[c]</sup> Jan-Dierk Grunwaldt,<sup>[b, c]</sup> and Robert Güttel<sup>]\*[a]</sup>

The production of liquid hydrocarbons from syngas (CO and H<sub>2</sub>) via the combined Fischer-Tropsch (FT) synthesis and hydroprocessing (HP) is a promising strategy to provide valuable chemicals and fuels based on renewable feedstocks. High yields of liquid products are essential for industrial implementation since short-chain side products like methane and CO<sub>2</sub> reduce the overall carbon efficiency, which holds true especially for bi-functional Co/zeolite catalysts. In order to investigate the influence of the support material properties on the methane and CO<sub>2</sub> selectivities in the combined FT and HP reaction, we synthesized four well-defined catalyst materials with similar cobalt particle sizes. The active material is supported on either

meso- or microporous silicates or aluminosilicates. The catalytic properties are investigated in FT experiments at industrially relevant conditions (20 bar, 200–260 °C) and correlated with *in situ* x-ray absorption spectroscopy results to determine the chemical environment responsible for the selectivity observed. The origin of the high methane selectivity detected for crystalline and amorphous aluminosilicate was mainly traced back to the strong cobalt-support interactions. The high CO<sub>2</sub> selectivity, observed only for crystalline zeolite materials, is driven by the presence of oxidized cobalt species, while the acidic support in combination with micropores and possible overcracking leads to the observed drop in the C<sub>5+</sub> selectivity.

## Introduction

Climate change induced by greenhouse gases like CO<sub>2</sub> is a global concern.<sup>[1,2]</sup> Therefore, the energy transition to alternative CO<sub>2</sub>-neutral fuel sources for already existing infrastructure, or the production of valuable chemical products, is a strong focus of scientific research.<sup>[3–6]</sup> Consequently, the power-to-liquid (PtL) approach is widely discussed as an alternative for the production of liquid fuels from renewable electricity, CO<sub>2</sub> and H<sub>2</sub>O.<sup>[7,8]</sup> This process involves the Fischer-Tropsch (FT) synthesis among others, where the catalytic hydrogenation of CO leads to the production of long-chain hydrocarbons. During the so-

called low temperature FT reaction, the application of Co-based catalysts at reaction temperatures and pressures of 200–250 °C and 20–40 bar, respectively, leads predominantly to saturated hydrocarbons and H<sub>2</sub>O.<sup>[9]</sup> In industrial applications mainly long-chain paraffins and a low methane selectivity are desired, while the long-chain paraffins are subsequently hydrocracked over zeolite catalysts in a second reactor at temperatures between 250 and 350 °C to yield short-chain hydrocarbons for the use as liquid fuel.<sup>[10]</sup> The combination of a FT catalyst and an active material for hydroprocessing (HP) in one single reactor requires a compromise between the optimal conditions for each reaction but is currently widely discussed in scientific literature with remarkable success.<sup>[9,11,15]</sup> Different concepts are for example the usage of catalyst layers<sup>[10,16]</sup> or physical mixtures<sup>[10,11,16]</sup> as well as the impregnation of zeolites<sup>[13,17,22]</sup> as support materials. An alternative approach is the encapsulation of the active material or catalyst particle inside a zeolitic membrane to ensure proximity of the active sites, stabilize the active nanoparticles and create an additional stay zone for the hydrocarbon products leading to increased residence times in the reactor.<sup>[12,14,23,24]</sup> Li et al.<sup>[14]</sup> studied Co/zeolite-Y catalysts encapsulated within a SiO<sub>2</sub> shell compared to zeolite-Y@SiO<sub>2</sub> materials impregnated with cobalt. The authors report high selectivities towards short-chain products and CO<sub>2</sub> for the former and a significant improvement of the C<sub>5</sub>–C<sub>11</sub> selectivity for the latter material. Javed et al.<sup>[24]</sup> designed a zeolite-based capsule catalyst by encapsulation of Co/ZSM-5 with a microporous silicalite-1 shell to create an additional retention zone for both reactants as well as hydrocarbons. The results show high CO conversion and gasoline range hydrocarbon selectivity at low CO<sub>2</sub> and CH<sub>4</sub> selectivities. Another approach is demon-

[a] Dr. A. Straß-Eifert, Dr. H. Becker, Dr. J. Friedland, Prof. R. Güttel  
Institute of Chemical Engineering  
Ulm University  
Albert-Einstein-Allee 11  
D-89069 Ulm (Germany)  
E-mail: robert.guettel@uni-ulm.de

[b] Dr. T. L. Sheppard, Prof. J.-D. Grunwaldt  
Institute for Chemical Technology and Polymer Chemistry  
Karlsruhe Institute of Technology  
Engesserstraße 20  
76131 Karlsruhe (Germany)

[c] Dr. T. L. Sheppard, Dr. A. Zimina, Prof. J.-D. Grunwaldt  
Institute of Catalysis Research and Technology  
Karlsruhe Institute of Technology  
Hermann-von-Helmholtz Platz 1  
76344 Eggenstein-Leopoldshafen (Germany)

 Supporting information for this article is available on the WWW under <https://doi.org/10.1002/cctc.202101053>

 © 2021 The Authors. ChemCatChem published by Wiley-VCH GmbH. This is an open access article under the terms of the Creative Commons Attribution Non-Commercial License, which permits use, distribution and reproduction in any medium, provided the original work is properly cited and is not used for commercial purposes.

strated by Liu et al.,<sup>[25]</sup> who used a conventional Co/SiO<sub>2</sub> catalyst as precursor and silica source in hydrothermal synthesis method to embed or confine Co<sub>3</sub>O<sub>4</sub> into the zeolite crystals. These catalyst materials presented a significantly higher gasoline selectivity and produced more iso-paraffins compared to conventional Co/SiO<sub>2</sub> and zeolite-supported catalysts. The authors attributed this observation to the confined reaction environment, the high diffusion efficiency, and the suitable acidic properties.

One main challenge using zeolite materials is the micropore structure and the accompanying diffusion limitation during the reaction. Therefore, another promising material class for bifunctional catalysts for the single-stage FT process are mesoporous, amorphous aluminosilicates, because of their high specific surface area, large pore volume and moderate acidity.<sup>[26]</sup> Up to now, only a few reports on the usage of these materials exist. Hwang et al.<sup>[27]</sup> confined Ru nanoparticles inside ordered mesoporous aluminosilicates with different Si/Al ratios (10, 30 and 50). The authors reported that with increasing Al content the acidity of the support material and the metal-support interaction increase, which leads to a decrease of the Ru reducibility. The catalyst material with Si/Al=50 exhibited the highest selectivity towards liquid fuels (C<sub>5</sub>–C<sub>20</sub>; 63.6%) and an excellent FT activity due to the mild acidity and relatively good reducibility. Cobalt nanoparticles supported on aluminosilicates and the effect of the particle size as well as promoters for the single-stage FT reaction were investigated by Lapidus et al.<sup>[28]</sup> The authors observed an increase in the reaction rate for cobalt crystallites larger than 8–13 nm. They further found that the promotion with CeO<sub>2</sub> increases the catalytic activity, although the selectivity towards the C<sub>5+</sub> hydrocarbon products is slightly decreased. As there are very few recent publications on the use of aluminosilicates, detailed investigations of the material properties linked to FT performance are currently missing.

Nevertheless, the material combinations discussed above are often reported to suffer from high methane selectivities and in some cases high CO<sub>2</sub> formation.<sup>[17,18,25,29,31]</sup> A variety of possible reasons are reported in literature. Especially for microporous zeolitic materials, the H<sub>2</sub>/CO ratio in the proximity of cobalt metal sites can be significantly higher than the ratio in the external gas phase due to a severe diffusion barrier affecting the CO molecules.<sup>[32,35]</sup> This higher H<sub>2</sub>/CO ratio is advantageous to the generation of methane.<sup>[36]</sup> Furthermore, unreduced cobalt oxide phases are able to catalyse the water-gas shift (WGS) reaction (CO + H<sub>2</sub>O → CO<sub>2</sub> + H<sub>2</sub>), further increasing the H<sub>2</sub>/CO ratio.<sup>[37]</sup> Additionally, smaller cobalt particles are reported to support the formation of short-chain hydrocarbons and hence promote methane formation.<sup>[38,39]</sup> Other factors can also contribute to a high methane selectivity like the existence of weak CO adsorption sites,<sup>[40]</sup> the hydrogenolysis of preferably heavier paraffins, which causes the successive demethylation forming methane and a heavier fragment,<sup>[41,42]</sup> as well as cobalt support interactions.<sup>[43]</sup> Several of these effects may be superimposed and therefore the specific cause of high methane selectivity is still a matter of debate.

Here, we applied a bottom-up strategy for the synthesis of well-defined Co particles supported inside and outside meso-

porous or microporous support materials, which allows tuning material properties such as the cobalt particle size. For this purpose, we have synthesized four different silicate-based materials offering micro- or mesoporosity and containing Al or not, to investigate the influence of the support materials in the FT synthesis. The materials were thoroughly investigated with transmission electron microscopy (TEM), scanning electron microscopy (SEM), X-ray diffraction (XRD), N<sub>2</sub>-physisorption, H<sub>2</sub> temperature-programmed reduction (H<sub>2</sub>-TPR), ammonia temperature-programmed desorption (NH<sub>3</sub>-TPD) and elemental analysis. FT experiments were performed under industrially relevant conditions on a custom-designed FT plant equipped with a fixed bed reactor. Particular focus was laid on the correlation of methane and CO<sub>2</sub> selectivities to the structural properties of the selected catalytic materials. Additionally, *in situ* X-ray absorption spectroscopy (XAS) experiments were conducted and linked with the FT experiments to investigate the Co particle stability, reducibility, and the influence of the different support materials on the methane and CO<sub>2</sub> selectivities.

## Experimental

### Material synthesis

The material synthesis route follows a bottom-up procedure as previously described.<sup>[44,45]</sup> In the first step polymer-stabilized cobalt oxide nanoparticles were prepared via solvothermal synthesis in ethanolic suspension. Subsequently, the cobalt oxide particles were encapsulated in either a mesoporous silica or aluminosilicate shell, yielding Co@mSiO<sub>2</sub> or Co@mSi<sub>x</sub>Al<sub>y</sub>O<sub>z</sub> core-shell particles, respectively. For the synthesis of Co@mSiO<sub>2</sub>, 50 g of the cobalt oxide suspension and 1.95 g cetyltrimethylammonium bromide (CTAB, high purity grade, AMRESCO) as porogen were dissolved in an ethanol/water (60/40-volume) mixture. The pH was adjusted to about 8.8 via the addition of 12.4 mL aqueous ammonia solution (NH<sub>3</sub><sub>aq</sub>, 30% p.a. ACS, CARL ROTH) and 6.40 mL tetraethyl orthosilicate (TEOS, for synthesis, MERCK) were added dropwise under stirring. After a reaction time of 2 h at room temperature, the solids were washed and collected via centrifugation, and afterwards calcined in air at 500 °C (heating rate 2 Kmin<sup>-1</sup>) for 6 h. To synthesize Co@mSi<sub>x</sub>Al<sub>y</sub>O<sub>z</sub>, 5.7 g Mowiol (Polyvinyl alcohol 4–98, MERCK) were dissolved in about 80 mL of H<sub>2</sub>O under stirring at 80 °C. After the addition of 0.03 g of sodium aluminate to achieve a Si/Al ratio of 100, the mixture was weighed, and the residual amount of water was added to reach 188.8 g in total. The pH was adjusted to about 8.8 by the addition of 12.4 mL NH<sub>3</sub> solution (NH<sub>3</sub><sub>aq</sub>, 30% p.a. ACS, CARL ROTH). Afterwards, 180 g of cobalt oxide suspension and 2.85 g CTAB (high purity grade, AMRESCO) as porogen were added under stirring. Subsequently, 15.1 mL of TEOS were added dropwise to the reaction mixture and it was stirred for 2 h at room temperature. The resulting particles were separated and washed via centrifugation, and afterwards calcined in air at 500 °C (heating rate 2 Kmin<sup>-1</sup>) for 6 h.

In the third step, Co@silicalite-1 or Co@HZSM-5 were produced via hydrothermal synthesis. Therefore, either Co@mSiO<sub>2</sub> or Co@m-Si<sub>x</sub>Al<sub>y</sub>O<sub>z</sub> were used as precursor materials and dissolved in an aqueous mixture of ammonia (NH<sub>3</sub><sub>aq</sub>, 30% p.a. ACS, CARL ROTH), tetrapropylammonium hydroxide (TPAOH, 40% w/w aq., ALFA AESAR) as structure-directing agent and nitric acid (0.1 M, for analysis, MERCK) for adjusting the pH to about 9. The reaction

mixture for synthesis of Co@HZSM-5 from Co@mSi<sub>x</sub>Al<sub>y</sub>O<sub>z</sub> exhibits a molar ratio of 1.0000 SiO<sub>2</sub> : 0.0050 Al<sub>2</sub>O<sub>3</sub> : 0.0283 NH<sub>4</sub><sup>+</sup> : 0.4113 TPAOH : 0.0392 HNO<sub>3</sub> : 41.6558 H<sub>2</sub>O : 0.4004 OH<sup>-</sup>, while it is 1.0000 SiO<sub>2</sub> : 0.0283 NH<sub>4</sub><sup>+</sup> : 0.4113 TPAOH : 0.0392 HNO<sub>3</sub> : 41.6558 H<sub>2</sub>O : 0.4004 OH<sup>-</sup> for synthesis of Co@silicalite-1 from Co@mSiO<sub>2</sub> without aluminium. After reaction at 175 °C for 30 h in a Teflon-lined autoclave, the products were purified with distilled water and collected via centrifugation. Afterwards, the resulting materials were calcined in air at 500 °C (heating rate 2 K min<sup>-1</sup>) for 6 h.

### Characterization methods

TEM images were obtained with a JEOL 1400 microscope operating at 120 kV. The samples were prepared by suspending the powder catalysts in ethanol via ultrasonication. Afterwards, one droplet of the suspension was applied on a graphitized copper grid (200 mesh). For statistical evaluation around 220 particles were counted using the software ImageJ for image processing.<sup>[46]</sup> The cobalt oxide particle size was evaluated by calculation of the mean particle size and the corresponding standard deviation. The specific cobalt surface area related to the cobalt mass ( $CSA / m_{Co}^2 \text{ g}_{Co}^{-1}$ ) is estimated from the cobalt oxide particle size considering the shrinkage of particles during reduction of cobalt oxide to metallic cobalt ( $d_{Co} = 0.75 d_{Co_3O_4}$ )<sup>[47]</sup> and assuming a spherical particle geometry and the bulk density of metallic cobalt [Eq. (1)].

$$CSA = \frac{6}{\rho_{Co} \cdot d_{Co}} \quad (1)$$

The SEM measurements were conducted at a SmartSEM Supra 55VP electron microscope from Carl Zeiss SMT Ltd. The acceleration voltage used was 3–6 kV and the usage of an SE2 detector allowed the investigation of details at the surface. The samples were prepared by gluing solids to the sample holder with carbon tape. XRD measurements were performed at a STOE STADI-p diffractometer equipped with a DECTRIS MYTHEN 1 K strip detector. Cu–K $\alpha$  radiation (1.54184 Å) with 40 kV was used in a 2 $\theta$  interval of 0–70°2 $\theta$  in steps of 0.015°2 $\theta$ . The cobalt oxide particle size was approximated from XRD measurements by means of the Scherrer equation using full width at half maximum (FWHM) for the (311) reflection at 26.6°2 $\theta$ .

N<sub>2</sub>-physisorption experiments were carried out with a high-resolution Micromeritics 3Flex instrument at liquid nitrogen temperature (–196 °C). This device is equipped with a special micropore port including a 0.1 Torr pressure transducer for investigation of microporous materials. Prior to the measurement, the solid samples were degassed under vacuum at 300 °C for 4 h. Afterwards, the adsorption and desorption isotherms were recorded. For evaluation of the specific surface area, the Brunauer-Emmett-Teller (BET) measurement and Rouquerol method were applied. The mesopore evaluation was conducted using the Barret-Joyne-Halenda (BJH) method using the adsorption branch. The micropore size distribution was determined by the Horwath-Kawazoe model, while the overall pore size distribution was analysed via density functional theory (DFT). Standard parametrization for SiO<sub>2</sub>/aluminosilicate and MFI zeolites was used for all evaluation models. NH<sub>3</sub>-TPD was performed using a Micromeritics AutoChem 2990 instrument equipped with a thermal conductivity detector (TCD). Typically, about 100 mg of the sample was dried in a He flow at 550 °C. Subsequently, the sample was cooled to 100 °C in a He flow. Thereafter, pulses of 10 vol% NH<sub>3</sub>/He are contacted with the sample until saturation was reached. The temperature (100 °C) and He flow were maintained for 1 h. Afterwards, the sample was heated under He flow to 550 °C at a rate of 10 K min<sup>-1</sup>, while the desorption of ammonia was monitored by a TCD detector. H<sub>2</sub>-TPR was measured

on the Micromeritics 3Flex instrument. The samples were dried at 120 °C for 30 min in an Ar flow prior to the measurement. After cooling down to 50 °C and baseline stabilization, the gas was switched to 10 vol% H<sub>2</sub> in Ar and the temperature was ramped up to 850 °C with a linear heating rate of 10 K min<sup>-1</sup>. Quantitative analysis was conducted after calibration of the device via reduction of copper oxide.

The elemental analysis of the catalysts was executed by a combination of two analytical methods at Mikroanalytisches Labor Kolbe (Oberhausen, Germany). After drying and acidulation of the samples the Co content was determined by atomic absorption spectroscopy (AAS) with an AAS Model Analyst 200 from PerkinElmer. For the analysis of the Si and Al content, the samples were treated with a so-called Wurzschnitt acidulation and measured with a photometric method at a UV/VIS Model Specord 50 Plus from AnalytikJena.

### In Situ-XAS Measurements

X-ray absorption spectroscopy (XAS) measurements in terms of X-ray absorption near edge structure (XANES) and extended X-ray absorption fine structure (EXAFS) were performed at the Co K edge (7709 eV) at the CAT-ACT beamline of the KIT Synchrotron (Karlsruhe, Germany). CAT-ACT is equipped with a 2.5 T wiggler X-ray source, and a double crystal monochromator (Si111) was used to select the incident beam energy.<sup>[48]</sup> Higher harmonic rejection was performed using Rh-coated mirrors. Measurements were conducted in transmission geometry using ionization chambers for analysis of the incident beam and the transmitted beam intensity. A Co foil placed between the second and third ionization chambers was measured at the same time as the catalyst samples and was used to calibrate the Co K absorption edge position and align the measured spectra. The beam spot size on the sample was approximately 0.5x0.5 mm<sup>2</sup>.

Samples were loaded into quartz capillaries of 1 mm (in the case of Co@HZSM-5 and Co@mSiO<sub>2</sub>) or 1.5 mm (in the case of Co@m-Si<sub>x</sub>Al<sub>y</sub>O<sub>z</sub>) outer diameter, with a bed length of approximately 4–5 mm and the sample held in position by small glass wool plugs.<sup>[49]</sup> Co@silicalite-1 was not measured due to time constraints. The capillaries were placed in the *in situ* sample holder of CAT-ACT, consisting of a hot air blower (FMB Oxford GSB-1300) controlled via a Eurotherm temperature regulator. Gases were dosed using mass flow controllers (Bronkhorst), while high-pressure conditions were obtained by means of a back pressure regulator (Bronkhorst). The temperature was read before X-ray measurements with a portable type K thermocouple above and below the capillary, then taking an average of these values. The following conditions were applied, and corresponding measurements performed:

- (i) reduction step (10 mL min<sup>-1</sup>, 100% H<sub>2</sub>) in which EXAFS was recorded first at ambient temperature, before heating to 400 °C (10 K min<sup>-1</sup> ramp rate) whilst continuously recording XANES. The temperature was held at 400 °C for approximately 30 min, before cooling to 150 °C and recording a further EXAFS spectrum.
- (ii) activation step (10 mL min<sup>-1</sup>, 2:1 H<sub>2</sub>:CO) in which EXAFS was recorded under syngas environment first at 150 °C and ambient pressure, before pressurizing the capillary from 1 to 20 bar whilst continuously recording XANES. On reaching 20 bar under syngas environment, a further EXAFS spectrum was recorded.
- (iii) FT reaction conditions (10 mL min<sup>-1</sup>, 2:1 H<sub>2</sub>:CO, 20 bar) in which XANES was recorded continuously whilst heating the sample from 150 to 260 °C (2 K min<sup>-1</sup> ramp rate) at 20 bar pressure. On reaching the final reaction temperature, EXAFS

scans were recorded continuously for up to 4 h, the reactor was then depressurized to 1 bar.

- (iv) second reduction step (10 mL min<sup>-1</sup>, 100% H<sub>2</sub>) in which the sample was heated from 260 to 400 °C (10 K min<sup>-1</sup> ramp rate) whilst continuously recording XANES. A final EXAFS spectrum was acquired at 400 °C.

During XAS experiments, the reactor outlet lines were heated to approximately 90 °C to limit condensation of FT waxes and long-chain products. A solvent trap containing cyclohexane at ambient temperature was placed immediately downstream of the back pressure valve (therefore at ambient pressure) furthermore to dissolve long-chain products from the gas stream. Despite these efforts, presumed high catalytic activity from the use of pure syngas did lead to the condensation of unidentified FT products in the reactor outlet pipes, leading to unstable pressure conditions during the reaction. In particular, blocking of the pressure gauge installed downstream the reactor causes a decrease in the apparent pressure measured. To mitigate this effect, the gas pipes were periodically heated with a portable hot air gun until bubbling in the solvent trap was visible. The gas phase components were sampled by mass spectrometry (Pfeiffer Vacuum Omnistar), to verify the correct gaseous environment and ensure no leaks were present. Product quantification was not possible due to unstable pressure conditions. Safety note: the use of pure CO and/or H<sub>2</sub> in quartz capillary microreactors is potentially dangerous. Equipment should always be thoroughly tested for leaks and stability at the desired pressure before performing synchrotron studies. The use of gas sensors is also essential to avoid a potential release of toxic and explosive gas mixtures.

The fractions of (metallic) Co<sup>0</sup>, CoO and Co<sub>3</sub>O<sub>4</sub> in the *in situ* XANES spectra were estimated using linear combination fitting (LCF) for references implemented in ATHENA software.<sup>[50]</sup> As reference spectra for fitting the experimental ones of CoO and Co<sub>3</sub>O<sub>4</sub> as standards for Co oxide (pressed as pellets), and Co foil to represent metallic Co<sup>0</sup> (details, see supporting information, SI) were used. All spectra were normalized to an edge step value of 1 before LCF analysis. Structure refinement was performed using ARTEMIS software (IFEFFIT).<sup>[50]</sup> The theoretical data were then adjusted to the first shell of the experimental spectra by the least square method in R-space between 1.5 and 2.8 Å. Further information on the analysis of the EXAFS data, curve fitting and statistics are provided in the SI.

### Catalytic FT synthesis experiment

The catalytic performance of the materials for FT synthesis was evaluated in a continuously operated reaction setup equipped with a tubular fixed-bed reactor (6.35 mm O.D., GHSV = 6 m<sup>3</sup> kg<sub>cat</sub><sup>-1</sup> h<sup>-1</sup>). The axial temperature profile was measured by a moveable type K thermocouple placed in a concentric capillary inside of the reactor. Prior to the experiment the catalyst powders were pelletized and sieved to a fraction of 100–200 μm, of which about 250 mg was loaded into the reactor, diluted with glass beads of 100–200 μm. Cobalt oxide was reduced *in situ* to metallic cobalt with pure H<sub>2</sub> (3 L<sub>STP</sub> h<sup>-1</sup>) at ambient pressure and 350 °C for 16 h (heating rate 5 K min<sup>-1</sup>). Afterwards, the reactor was cooled down in hydrogen flow to 150 °C. For activation of the catalyst, the gas flow was switched to syngas (H<sub>2</sub>/CO ratio of 2) with a CO flow rate of 0.5 L<sub>STP</sub> h<sup>-1</sup> and the reactor was subsequently pressurized to 20 bar. The activation was executed stepwise from 150 to 200 °C in 10 K steps each holding for 12 h. The FT experiments were performed afterwards at reaction temperatures of 200, 220, 240 and 260 °C. Note that the catalytic test of each material is denoted as campaign, while each set of operating conditions studied is referred to as experiment. The gaseous and volatile products were analysed

with an online GC (Shimadzu, GC2010) using Ar as internal standard (dosed at 10 vol% premixed with CO, as described in Knochen et al.<sup>[51]</sup>). While the permanent gases and methane were analysed using a serial connection of a RT-Q-Bond column (30 m, 0.53 mm, 20 μm ID), a MS 5 A PLOT column (30 m, 0.53 mm, 50 μm ID) and a thermal conductivity detector (TCD), the C<sub>1+</sub> hydrocarbons were analysed with a flame ionization detector (FID) after separation with a RT-Q-Bond column. The liquid products were collected in a wax and water separator operated at 0 and 150 °C, respectively, followed by separation of water and hydrocarbons by decantation and determination of the respective amounts by weighing. The hydrocarbon samples are analysed with an offline-GC (Thermo-Fisher, TRACE 1300) equipped with a DB-2887 column (10 m, 0.53 mm, 3 μm ID) and a FID.

Each experiment was studied for a specific time period until the steady-state criterion defined in Equation (2) was reached. The left side of the equation corresponds to the change in CO conversion between consecutive online GC analyses (sampling time 30 min), while X<sub>CO,max</sub> refers to the maximum CO conversion detected within the respective experiment. This criterion therefore restricts the loss in conversion under steady-state conditions to below 1% of the maximum conversion within 24 h time on stream (TOS) for each experiment, which ensures that the reaction is sufficiently stable. The FT data given below represents a mean value of the last 4 h TOS (8 sample points) at steady-state conditions.

$$\left| \frac{\Delta X_{\text{CO}}}{\Delta t} \right| \leq 0.004 X_{\text{CO,max}} \quad (2)$$

## Results and Discussion

### Material preparation and characterization results

In Figure 1, the representative TEM and SEM images of the as-synthesized catalyst materials are presented. Additional TEM images, also of zeolite crystal slices, can be found in the SI (Figure S1). The materials are arranged in order to indicate the different properties like crystallinity, acidity, and porosity. On the right side of the figure, the schematic synthesis pathway is indicated using the colour code introduced here for the specific materials. Note that the main difference compared to our earlier studies is that the H-ZSM-5 material is synthesized based on Co@mSi<sub>x</sub>Al<sub>y</sub>O<sub>z</sub> as a precursor providing a Si/Al ratio of 100. Thus, Al is already present in the precursor and no additional Al-source was used. The TEM images of Co@mSiO<sub>2</sub> (Figure 1a) and Co@mSi<sub>x</sub>Al<sub>y</sub>O<sub>z</sub> (Figure 1b) reveal spherically shaped particles of uniform core-shell architecture. In both cases the thickness of the shell is about 50 nm, leading to a size of the individual core-shell particles of about 170 nm. The SEM images of Co@silicalite-1 (Figure 1, c) and Co@HZSM5 (Figure 1, d) show comparable zeolite crystals with about 1–2 μm in size. Furthermore, non-encapsulated cobalt nanoparticles and sheet-like structures indicative of Co-silicate species are detected at the surface of the zeolite crystals.<sup>[52]</sup>

In Table 1, the characterization results related to the FT active phase cobalt and the precursor-phase cobalt oxide are summarized. The cobalt oxide particle sizes evaluated via TEM (see SI, Figure S2) for Co@mSiO<sub>2</sub> and Co@mSi<sub>x</sub>Al<sub>y</sub>O<sub>z</sub> are about 40 nm, while for Co@silicalite-1 and Co@HZSM5 a particle size of about 34 nm is found. The difference in size may be caused

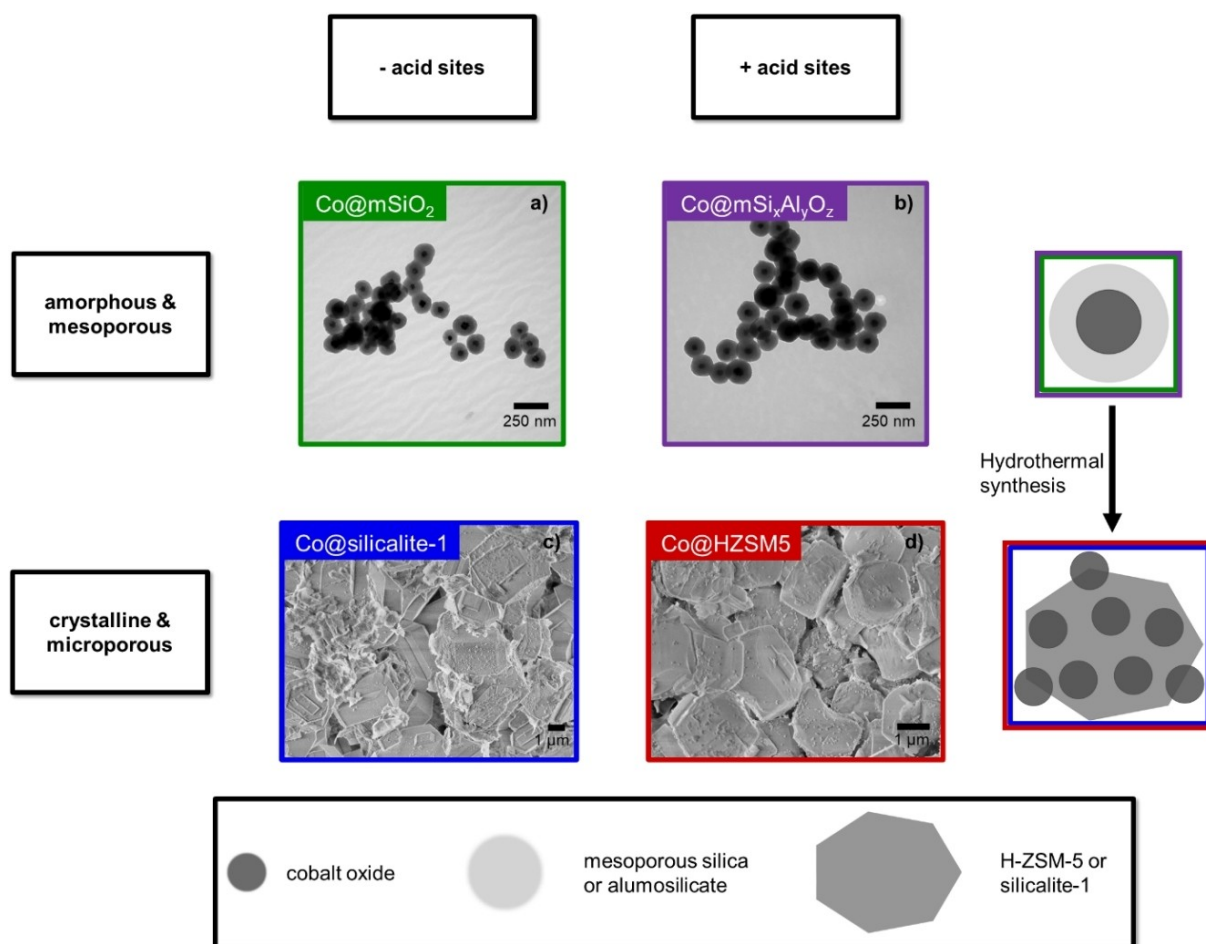


**Figure 1.** Representative TEM or SEM images of the catalyst materials Co@mSiO<sub>2</sub> (a), Co@mSi<sub>x</sub>Al<sub>y</sub>O<sub>z</sub> (b), Co@silicalite-1 (c) and Co@HZSM5 (d) with an indication of the material properties in the boxes; the sign preceding the term 'acid sites' means that those sites are either present (+) or not present (-); schematic synthesis route (right) and corresponding legend (bottom).

Catalyst	$d_{\text{Co}_3\text{O}_4}$ [nm]	XRD	$w_{\text{Co}}$ [wt %]		$w_{\text{Co}}$ [wt %]	CSA <sup>[d]</sup> [m <sup>2</sup> g <sup>-1</sup> ]
	TEM		total	silicate		
Co@mSiO <sub>2</sub>	39.1 ± 7.3	29.9	8.7	0	8.1	23.0
Co@mSi <sub>x</sub> Al <sub>y</sub> O <sub>z</sub>	42.1 ± 7.6	29.5	8.2	0	7.9	21.3
Co@silicalite-1	33.9 ± 6.5	30.8	7.2	1.8	8.2	26.5
Co@HZSM5	33.9 ± 7.1	29.6	8.1	2.2	8.2	26.5

[a] Cobalt oxide particle size determined via TEM with error bars representing the standard deviation and via XRD, [b] Total cobalt mass fraction determined via H<sub>2</sub>-TPR, [c] Total cobalt mass fraction determined via ICP, [d] Specific cobalt surface area calculated from cobalt particle size (TEM); see Experimental Section.

by partial cobalt leaching in the strong basic media during the hydrothermal synthesis. In contrast, the estimated particle sizes based on XRD data are comparable among all materials studied but smaller than the values obtained via TEM. The difference between TEM and XRD results can be explained by the fact the crystallite sizes are obtained by XRD, which are not necessarily identical to the sizes of the cobalt core, showing additionally amorphous phases. The CSA amounts to about 22 m<sup>2</sup>g<sup>-1</sup> for Co@mSiO<sub>2</sub> and Co@mSi<sub>x</sub>Al<sub>y</sub>O<sub>z</sub> and to a slightly higher value of 26 m<sup>2</sup>g<sup>-1</sup> for the zeolitic materials, due to smaller cobalt particle

sizes observed by TEM. The quantitative evaluation of H<sub>2</sub>-TPR profiles (see SI, Figure S3) leads to a Co mass loading of about 7–9 wt%. The fraction of Co embedded in silicate structures is about 2–3 wt%, which are known<sup>[53]</sup> to be hardly reducible at temperatures below 600 °C as shown by TPR. The comparison of the results achieved via H<sub>2</sub>-TPR and the results via quantitative bulk analysis reveals comparable values for all catalyst materials.

The results of N<sub>2</sub>-physisorption measurements are summarized in Table 2 (for corresponding pore size distribution and

**Table 2.** Results of N<sub>2</sub>-physisorption, quantitative analysis and NH<sub>3</sub>-TPD.

Catalyst	$V_{\text{meso}}^{[a]}$ [cm <sup>3</sup> g <sup>-1</sup> ]	$d_{\text{meso}}^{[b]}$ [nm]	$d_{\text{micro}}^{[c]}$ [nm]	Si/Al <sup>[d]</sup> [mol/mol]	Si/Co <sup>[d]</sup> [mol/mol]	Al/Co <sup>[d]</sup> [mol/mol]	$n_{\text{acid}}^{[e]}$ [mmol g <sub>cat</sub> <sup>-1</sup> ]
Co@mSiO <sub>2</sub>	0.69	3.2	–	–	7.9	0.0033	–
Co@mSi <sub>x</sub> Al <sub>y</sub> O <sub>z</sub>	0.62	3.2	–	109	7.9	0.0727	0.12
Co@silicalite-1	0.06	3.1	0.54	–	8.5	0.0026	0.08
Co@HZSM5	0.06	3.1	0.54	1851	7.5	0.0041	0.16

[a] Mesopore volume obtained from the adsorbed total volume at 0.98 p/p<sup>0</sup> minus micropore volume determined via HK method, [b] Mesopore size via BJH adsorption isotherm, [c] Micropore size via HK method, [d] Atomic ratio determined via ICP, [e] Acid site density determined via NH<sub>3</sub>-TPD.

isotherms see SI, Figure S4). The mesopore volumes of about 0.6–0.7 cm<sup>3</sup>g<sup>-1</sup> determined for Co@mSiO<sub>2</sub> and Co@mSi<sub>x</sub>Al<sub>y</sub>O<sub>z</sub> are in good agreement. Furthermore, both materials exhibit a monomodal pore size distribution offering mesopores of 3.2 nm. The zeolitic materials (Co@silicalite-1 and Co@HZSM5) exhibit a bimodal pore size distribution with mesopores of 3.1 nm and micropores of 0.54 nm, the latter being characteristic for MFI zeolites. While the XRD results (see SI, Figure S5) confirm the successful crystallization of the amorphous aluminosilicate shell into zeolitic material during hydrothermal synthesis, the remaining mesopore volume indicates incomplete conversion.

The Si/Al ratio (109) is the lowest for Co@mSi<sub>x</sub>Al<sub>y</sub>O<sub>z</sub>, while the acidic H-ZSM-5 exhibits a twenty times higher value (1851). Thus, during the hydrothermal synthesis the Al content is decreasing drastically, probably due to the complexation of Al with TPAOH and insufficient Al incorporation.<sup>[54]</sup> Nevertheless, the Al content does not necessarily correlate with the acid site density determined by NH<sub>3</sub>-TPD as shown for Co@HZSM5, exhibiting a high Si/Al ratio and still a reasonable acidity. That is caused by the bulk method ICP, which does not distinguish between extra- and framework Al. The difference in acidity of Co@HZSM5 and Co@silicalite-1 corresponds well to the NH<sub>3</sub>-TPD profiles (see SI, Figure S6), exhibiting two distinct peaks corresponding to weak<sup>[55]</sup> and strong<sup>[56]</sup> acid sites for the former material, while for the other materials noisy profiles were recorded. The acidity of Co@HZSM5 is comparable to literature (typical:<sup>[57]</sup> Si/Al 100, 0.15 mmol g<sup>-1</sup>) as well as to our previous work (0.18 mmol g<sup>-1</sup>). The acidity for Co@mSi<sub>x</sub>Al<sub>y</sub>O<sub>z</sub> is slightly lower with a value of 0.12 mmol g<sup>-1</sup>. Interestingly, even for the Co@silicalite-1 catalyst, an acidity of 0.08 mmol g<sup>-1</sup> was detected. These results show that acidity determination in these composite materials is much more complicated than in zeolite-only materials, since cobalt oxide provides Lewis acidity, as well.

### In situ X-ray absorption spectroscopic studies at the Co K-edge

The oxidation state of the Co catalysts was studied by LCF of the XANES spectra obtained during TPR up to 400 °C. It should be noted that according to the TPR results this may not be expected to lead to complete reduction of the catalyst, which occurred above 450 °C in the case of Co@mSiO<sub>2</sub> and Co@mSi<sub>x</sub>Al<sub>y</sub>O<sub>z</sub>, and above 700 °C in the case of Co@silicalite-1 and Co@HZSM5. LCF fitting was performed using Co<sub>3</sub>O<sub>4</sub> and CoO

pellets as reference materials for cobalt oxide, and Co foil spectrum as reference material for metallic cobalt (Co<sup>0</sup>) (reference spectra given in SI). Although the Co foil spectrum acts as an external standard and may not ideally reflect the structure of small Co nanoparticles, it still allows monitoring the extent of the reduction more accurately for each catalyst. The LCF fitting and corresponding XANES spectra for Co@mSiO<sub>2</sub>, Co@mSi<sub>x</sub>Al<sub>y</sub>O<sub>z</sub> and Co@HZSM5 are shown in Figure 2. Error bars are derived from the LCF subroutine of the Athena 0.9.26 software tool.<sup>[50]</sup>

During TPR of both amorphous mesoporous samples Co@mSiO<sub>2</sub> and Co@mSi<sub>x</sub>Al<sub>y</sub>O<sub>z</sub>, an initial state resembling Co<sub>3</sub>O<sub>4</sub> was observed, which reduced via a CoO intermediate starting between 135 to 170 °C (Figure 2a–b). Metallic Co<sup>0</sup> was first observed at a slightly higher temperature of 170 to 220 °C. This is in good agreement with the laboratory TPR data reported in the SI (Figure S3), during which H<sub>2</sub> consumption was observed at around 200 °C, reflecting the appearance of Co<sup>0</sup> by XANES. This indicates the two-step reduction of Co<sub>3</sub>O<sub>4</sub> (initial catalyst state) via a CoO intermediate<sup>[58]</sup>, which may proceed either with H<sub>2</sub> or thermally in the absence of H<sub>2</sub>.<sup>[59]</sup> Further reduction to Co<sup>0</sup> appeared to be linked to H<sub>2</sub> consumption for the catalysts tested here. Since heating was performed at a ramp rate of 10 Kmin<sup>-1</sup> and a single XANES scan took around 90 s, one XANES scan was recorded every 16 K. LCF analysis of Co@mSiO<sub>2</sub> and Co@mSi<sub>x</sub>Al<sub>y</sub>O<sub>z</sub> indicates that the catalysts were mainly reduced during TPR, though the presence of some oxide species cannot be excluded based on the fits. This can be observed by considering the intensity ratio of the characteristic features at 7726 and 7734 eV following initial reduction (spectrum B), compared to the Co foil reference spectrum (Figure 2d–e). It should be noted that the TPR shown for Co@mSiO<sub>2</sub> (Figure 2a) is a result of two independent measurements on samples taken from the same Co@mSiO<sub>2</sub> catalyst batch, one in a 1 mm capillary, and one in a 1.5 mm capillary (see SI). As the composition of each catalyst batch was assumed to be identical and no reaction was taking place (only reduction), this approach is valid for the purposes of displaying a complete TPR profile.

XANES data extracted at several points during the complete experiment for Co@mSiO<sub>2</sub> (including syngas conditions, pressurisation to 20 bar, FT reaction, and final reduction) are shown in Figure 2d. Notably, following initial TPR during which the catalyst was reduced, no significant change in local coordination environment or oxidation state was observed at any point during activation in syngas at 150 °C or FT reaction up to 260 °C.

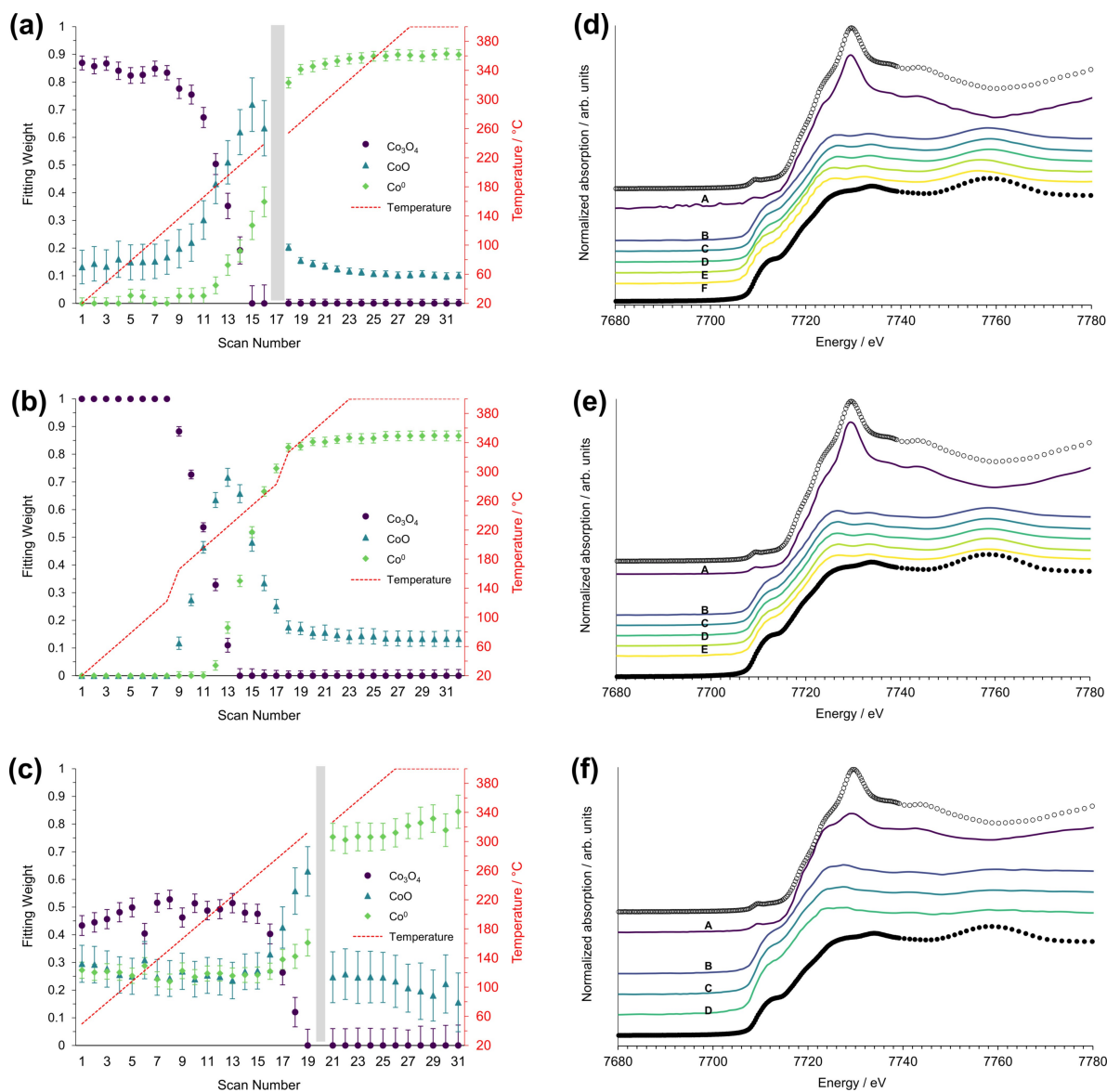


**Figure 2.** LCF of XANES data for: (a) Co@mSiO<sub>2</sub>; (b) Co@mSi<sub>0.5</sub>Al<sub>0.5</sub>O<sub>2</sub>; (c) Co@HZSM5 during TPR using Co<sup>0</sup> foil, Co<sub>3</sub>O<sub>4</sub> and CoO as standards. The grey bar indicates a break in the recording of XANES spectra. Normalized offset Co K edge XANES spectra for (d) Co@mSiO<sub>2</sub>; (e) Co@mSi<sub>0.5</sub>Al<sub>0.5</sub>O<sub>2</sub>; (f) Co@HZSM5 showing the catalyst: A – in initial state, B – after reduction at 400 °C in H<sub>2</sub>, C – under syngas at 150 °C and 20 bar pressure, D – under syngas at 260 °C and 20 bar pressure, E – under H<sub>2</sub> at 260 °C after 4 h FT reaction time, F – after final reduction at 400 °C in H<sub>2</sub>. Reference XANES spectra for Co<sub>3</sub>O<sub>4</sub> (hollow dots ○) and Co<sup>0</sup> (filled dots ●) are also shown above and below the catalyst XANES data.

This is evidenced by the high degree of similarity between spectra B to F in Figure 2d. During final reduction of the Co@mSiO<sub>2</sub> catalyst after reaction, a small shift in the edge position was observed. Essentially, the catalyst always appeared fully reduced after completion of the initial TPR at 400 °C according to XANES analysis. For Co@mSi<sub>0.5</sub>Al<sub>0.5</sub>O<sub>2</sub> similar results were obtained (Figure 2e). Although the intensity of the feature at 7726 eV was slightly greater for Co@mSi<sub>0.5</sub>Al<sub>0.5</sub>O<sub>2</sub> than for Co@mSiO<sub>2</sub> following TPR (spectrum B), after FT synthesis and a second reduction step (spectra C to F) the XANES spectra for both catalysts were essentially the same. In summary, the results indicate that while the catalysts may not have been fully reduced during the first reduction step, the Co<sup>0</sup> content

generally increased with sequential reduction steps and particularly after FT synthesis.

The data quality of XANES scans for Co@HZSM5 was generally lower than for the other catalysts tested, despite similar Co massloading, particle size, and capillary diameter (Figure 2f). As such the LCF analysis exhibits significantly greater error (Figure 2c). The initial state of the Co@HZSM5 catalyst was notably different from the dominant Co<sub>3</sub>O<sub>4</sub> character of Co@mSiO<sub>2</sub> and Co@mSi<sub>0.5</sub>Al<sub>0.5</sub>O<sub>2</sub> shown previously, in that an apparent mixture of Co<sub>3</sub>O<sub>4</sub>, CoO and metallic Co<sup>0</sup> were all initially fitted by LCF. However, this may indicate that the initial structure could not be accurately represented by the LCF standards used here. As with the other samples, a relative

increase in the CoO intermediate was detected at around 260 °C, which diminished to form Co<sup>0</sup> above this temperature.<sup>[60]</sup> The lower reducibility of Co@HZSM5 in comparison to the other samples tested supports the presence of Co-silicate type species.<sup>[52,60]</sup> Notably, it is unlikely that the catalyst was fully reduced after treatment at 400 °C in H<sub>2</sub>, due to the relatively large fraction of CoO species detected following reduction. This is supported by the TPR data shown in the SI (Figure S3) which showed a secondary H<sub>2</sub> consumption peak at 700 °C that was not reached during XAS experiments, indicative of Co species present in different chemical states. This is known to be the case for the Co@HZSM5 catalyst, where Co species encapsulated in the zeolite and those on the external surface may exhibit different reducibility.<sup>[61]</sup>

Additional XANES spectra recorded during activation in syngas and FT reaction are shown in Figure 2f. In this instance the final reduction step was not monitored by XANES due to time constraints. However, EXAFS data were recorded for all states of the Co@HZSM5 catalyst as discussed below. No differences in the XANES region were detected at any stage after the initial reduction, indicating the catalyst remained a mainly reduced state during FT synthesis. It should be noted that during initial TPR, the sample changed position slightly and the capillary holder had to be realigned with respect to the X-ray beam, therefore a short break in the consecutive XANES scans is indicated by the grey shaded area in Figure 2c. The sample was maintained under reducing conditions at approximately 300 to 330 °C during this interval.

To further investigate the presence of possible oxidic character before, during and after FT synthesis for each catalyst, EXAFS data were also recorded and fitted to theoretical models of Co<sup>0</sup> and CoO generated by FEFF code (see SI for further details on EXAFS).<sup>[50]</sup> The statistics of the EXAFS fitting are shown in Table 3. For both Co@mSiO<sub>2</sub> and Co@mSi<sub>x</sub>Al<sub>y</sub>O<sub>z</sub>, an excellent first shell fitting was obtained simply by modelling the Co–Co bonding in metallic cobalt. This character was observed for all measurement conditions following the initial reduction, meaning that the catalysts were most probably mainly or fully reduced during FT synthesis even at 20 bar pressure. It should

be noted that the temperature at which EXAFS scans were recorded was not uniform, which is reflected by the trend of increasing value and error in the Debye-Waller term ( $\sigma^2$ ). No contribution to the coordination number at a typical Co–O bond distance is found for first shell fitting of oxygen since including oxygen in any of the fits was detrimental to the overall quality. The results of fitting for Co@HZSM5 in terms of coordination number and statistical confidence were notably different from the other samples tested. Again, the inclusion of oxygen was generally detrimental to the quality of the fit, indicating that the minor structural differences, which may be present between the amorphous mesoporous samples (Co@mSiO<sub>2</sub> and Co@mSi<sub>x</sub>Al<sub>y</sub>O<sub>z</sub>) and Co@HZSM5, are possibly not attributable to a partially oxidised sample. Notably, the coordination numbers for Co in the Co@HZSM5 sample were dramatically lower than both the expected values for larger Co particles of 50 nm (e.g., CN=12) and lower compared to the Co@mSiO<sub>2</sub> and Co@mSi<sub>x</sub>Al<sub>y</sub>O<sub>z</sub>. As the Co particle size observed by both TEM and XRD and cobalt loading for all tested catalysts was relatively uniform within the typical error (Table 1), the relatively higher inaccuracy of the fitting model for Co@HZSM5 cannot be explained by differences in particle size. Additional fits (see SI) were performed on the second shell using Co–Si paths extracted from a structural model of beta cobalt silicate (Co<sub>2</sub>SiO<sub>4</sub> ICSD 8132), to which an acceptable fit was found for the Co@HZSM5 catalysts during the second reduction stage after FT synthesis. This supports the observation of Co silicate type species from TEM, and the indicated presence of these species during TPR. The exact Co-silicate species formed cannot be determined based on the EXAFS results, but nevertheless indicate the probable presence of such species. It should further be noted that XAS is a bulk measurement technique and is therefore unable to distinguish between differences resulting from Co present in diverse chemical environments on the same sample. For example, bulk XAS cannot differentiate the difference between Co encapsulated in the zeolite and that present on the external surface. Where such species may react differently to the chemical environment present, this may lead to an

**Table 3.** Structural parameters determined from fitting of the Co K edge EXAFS data for Co@mSiO<sub>2</sub> and Co@mSi<sub>x</sub>Al<sub>y</sub>O<sub>z</sub> and Co@HZSM5 under different experimental conditions.<sup>[a]</sup>

Catalyst	Conditions	CN / Co	$d_{\text{Co-Co}}$ [Å]	$\sigma^2$ [10 <sup>-3</sup> Å <sup>2</sup> ]	$\delta E0$ [eV]	$\rho$ [%]
Co@mSiO <sub>2</sub> , 1 mm capillary	Reduction-I, 400 °C	10.1 ± 0.38	2.49 ± 0.00	8.1 ± 0.4	6.54 ± 0.38	< 0.1
	Activation, 150 °C	–	–	–	–	–
	FT synthesis, 260 °C	10.3 ± 0.48	2.49 ± 0.00	10.4 ± 0.5	6.07 ± 0.46	0.1
Co@mSi <sub>x</sub> Al <sub>y</sub> O <sub>z</sub> , 1.5 mm capillary	Reduction-II, 400 °C	9.9 ± 0.60	2.49 ± 0.00	12.6 ± 0.7	5.76 ± 0.58	0.4
	Reduction-I, 400 °C	9.3 ± 0.81	2.50 ± 0.01	7.95 ± 0.87	7.35 ± 0.87	0.3
	Activation, 150 °C	–	–	–	–	–
Co@HZSM5, 1.5 mm capillary	FT synthesis, 260 °C	9.5 ± 0.57	2.49 ± 0.00	10.0 ± 0.64	6.70 ± 0.59	0.2
	Reduction-II, 400 °C	8.9 ± 0.59	2.48 ± 0.01	12.0 ± 0.00	5.52 ± 0.65	0.4
	Reduction-I, 400 °C	2.0 ± 0.82	2.49 ± 0.03	7.2 ± 3.8	7.18 ± 4.12	6.3
	Activation, 150 °C	2.2 ± 0.72	2.49 ± 0.02	2.7 ± 2.7	6.35 ± 3.55	3.9
	FT synthesis, 260 °C	1.8 ± 0.64	2.49 ± 0.02	4.3 ± 3.2	6.49 ± 3.80	4.9
	Reduction-II, 400 °C	2.3 ± 0.73	2.48 ± 0.02	1.5 ± 2.3	5.97 ± 3.37	3.3

[a]  $S_{02} = 0.737$  from fitting theoretical model of Co<sup>0</sup> to the experimental spectrum of Co foil; CN: coordination number;  $d$ : bond distance;  $\sigma^2$ : Debye-Waller factor;  $\delta E0$ : energy shift;  $\rho$ : misfit.

averaging of the different chemical states observed by XAS and therefore increased error.

### Catalytic Performance in Fischer-Tropsch Synthesis

For comparison of the catalytic activity and selectivity, the CO conversion and cobalt time yield (CTY) being the cobalt specific CO conversion rate as well as the CO<sub>2</sub> and hydrocarbon selectivities were determined at different reaction temperatures. The results of the catalytic measurements in FT synthesis are summarized in Table 4. The CO conversion and thus the CTY is increasing with rising temperature as expected from Arrhenius law (see SI, Figure S13). The corresponding apparent activation energies are obtained from CTY values for different temperature ranges (see SI, Table S2 and Figure S14). While the amorphous materials exhibit values in the range of 60 to 85 kJ mol<sup>-1</sup>, which is in good agreement with previous work and literature,<sup>[45,62,63]</sup> the range for the zeolitic materials is lower and broader. In particular, the apparent activation energy drops at temperatures above 240 °C, indicating either mass transfer issues, changes in the dominant reaction pathway or reaction mechanism occurring at higher temperatures. Additionally, slow deactivation processes, such as water-induced cobalt oxidation or coking, might affect the apparent activation energy as well.<sup>[64,64,66]</sup> A significant growth of cobalt particles can be ruled out by *ex situ* TEM experiments of spent catalysts samples, which in general show decreased particle sizes compared to the fresh catalysts. This is probably due to the presence of metallic Co in the spent catalysts rather than Co<sub>3</sub>O<sub>4</sub> present in the fresh catalysts as confirmed by XRD (see SI, Figure S15 and S16). Note that steady state is defined to be reached if the activity loss is below a certain threshold as explained in the experimental section [see Eq. (2)]. Therefore, slow changes in activity might still contribute to the apparent activation energy.

At temperatures between 200 and 240 °C the materials can clearly be distinguished between those with and those without

Al. In particular, Co@mSi<sub>x</sub>Al<sub>y</sub>O<sub>z</sub> and Co@HZSM5 containing Al, exhibit about two times higher CTY values. With temperature, the CTY raises for all materials exhibiting a maximum for Co@mSi<sub>x</sub>Al<sub>y</sub>O<sub>z</sub> at 260 °C, while the value for Co@HZSM5 remains constant above 240 °C. The obtained CTY values are in good agreement with our own results reported earlier<sup>[44,45]</sup> and with literature values. For instance, Khang et al.<sup>[20]</sup> reported 1.7 and 5.6 · 10<sup>-5</sup> mol<sub>CO</sub> g<sub>Co</sub><sup>-1</sup> s<sup>-1</sup> for Co/SiO<sub>2</sub> and 0.6 and 2.7 · 10<sup>-5</sup> mol<sub>CO</sub> g<sub>Co</sub><sup>-1</sup> s<sup>-1</sup> for Co/HZSM5 at 220 and 240 °C, respectively, while Sartipi et al.<sup>[67]</sup> detected about 7.2 · 10<sup>-5</sup> mol<sub>CO</sub> g<sub>Co</sub><sup>-1</sup> s<sup>-1</sup> for Co/SiO<sub>2</sub> and 13.0 · 10<sup>-5</sup> mol<sub>CO</sub> g<sub>Co</sub><sup>-1</sup> s<sup>-1</sup> for Co/mHZSM5 at 240 °C and 15 bar. The high CTY for Co@mSi<sub>x</sub>Al<sub>y</sub>O<sub>z</sub> is surprising since the material is comparable to Co@mSiO<sub>2</sub> in terms of Co mass loading, Co particle size and pore volume and only differs in the additional presence of Al. Furthermore, research groups reported in literature that aluminosilicates exhibit a comparably low catalytic activity,<sup>[27,28]</sup> which is in contrast to our findings.

The selectivity towards CO<sub>2</sub>, methane and higher hydrocarbons is depicted in Figure 3. Note that the conversion differs to a certain extent, which may also affect the observed selectivities. However, at each individual temperature point the conversion range among the different materials is much narrower, and therefore appropriate for comparison of the selectivities among the materials at similar conversion levels. The temperature effect on the selectivity, in contrast, is superimposed to a certain extent by the change in conversion. We, therefore, discuss this effect qualitatively with respect to the comparison between the materials used. The CO<sub>2</sub> selectivity shows an increasing trend with temperature. The correlated raising CO conversion leads to an increasing water vapor pressure, which favours the WGS reaction and thus CO<sub>2</sub> formation as suggested in literature reports.<sup>[64]</sup> Co@silicalite-1 and Co@HZSM5 exhibit rather high values at 260 °C compared to the amorphous materials. Most probably, the limited diffusion of H<sub>2</sub>O from the formation site through the microporous zeolitic structure into the gas phase leads to a higher fraction of H<sub>2</sub>O in proximity to the reactive sites, which

**Table 4.** CO conversion ( $X_{\text{CO}}$ ), cobalt time yield (CTY), and selectivity ( $S_i$ ) towards CO<sub>2</sub>, CH<sub>4</sub>, C<sub>2</sub>-C<sub>4</sub> and C<sub>5+</sub> of the catalyst materials at 200, 220, 240 and 260 °C after reaching steady state.<sup>[a]</sup>

$T$ [°C]	Catalyst material	$X_{\text{CO}}$ [%]	CTY [10 <sup>-5</sup> mol <sub>CO</sub> g <sub>Co</sub> <sup>-1</sup> s <sup>-1</sup> ]	$S_i$ [%]			
				CO <sub>2</sub>	C <sub>1</sub>	C <sub>2</sub> -C <sub>4</sub>	C <sub>5+</sub>
200	Co@mSiO <sub>2</sub>	3.4	1.1	0	6.6	5.5	87.9
	Co@mSi <sub>x</sub> Al <sub>y</sub> O <sub>z</sub>	4.4	1.4	0	10.2	7.6	82.2
	Co@silicalite-1	3.4	1.0	0	7.5	11.9	80.6
	Co@HZSM5	5.0	1.5	0	27.3	8.8	63.9
220	Co@mSiO <sub>2</sub>	5.4	1.7	0	12.4	9.2	78.4
	Co@mSi <sub>x</sub> Al <sub>y</sub> O <sub>z</sub>	9.4	2.9	0.5	17.0	10.9	71.6
	Co@silicalite-1	6.0	1.8	1.1	13.8	18.4	66.7
	Co@HZSM5	9.5	2.9	0.7	32.1	13.2	54.0
240	Co@mSiO <sub>2</sub>	12.1	3.6	1.1	19.4	13.9	65.6
	Co@mSi <sub>x</sub> Al <sub>y</sub> O <sub>z</sub>	20.2	6.3	0.7	24.0	14.5	60.8
	Co@silicalite-1	12.1	3.7	2.6	18.3	20.5	58.6
	Co@HZSM5	17.6	5.3	2.9	30.9	15.3	50.9
260	Co@mSiO <sub>2</sub>	25.6	7.8	1.4	27.0	19.9	51.7
	Co@mSi <sub>x</sub> Al <sub>y</sub> O <sub>z</sub>	35.2	11.0	1.0	30.3	16.2	52.5
	Co@silicalite-1	18.7	5.6	7.7	22.8	22.4	47.1
	Co@HZSM5	19.7	5.9	12.5	28.8	15.1	43.6

[a] Reaction conditions:  $p = 20$  bar, H<sub>2</sub>/CO = 2, gas hourly space velocity (GHSV) 6 m<sup>3</sup> kg<sub>cat</sub><sup>-1</sup> h<sup>-1</sup>.

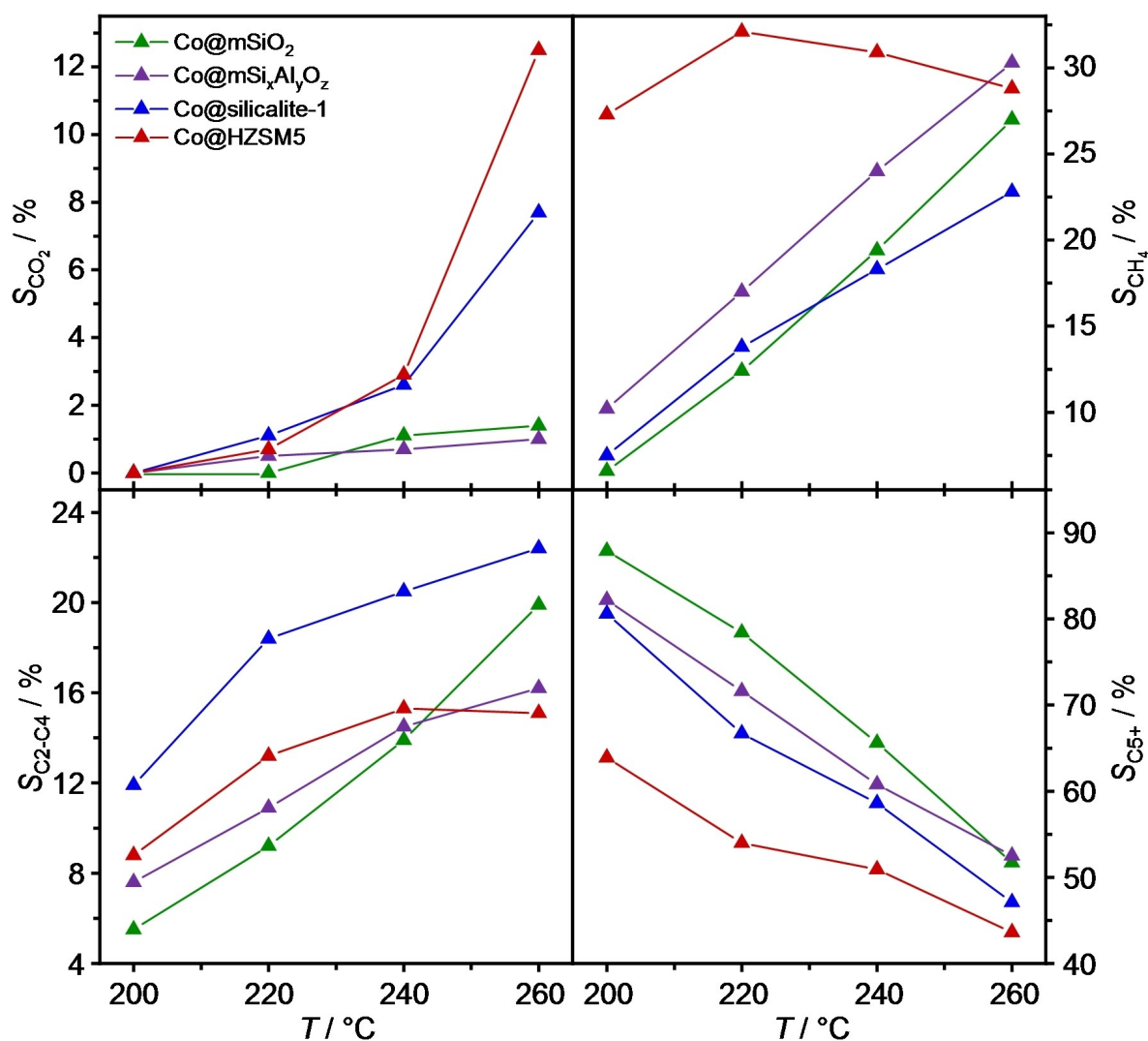


**Figure 3.** CO<sub>2</sub>, CH<sub>4</sub>, C<sub>2</sub>-C<sub>4</sub> and C<sub>5</sub>+ selectivity as a function of reaction temperature for Co@mSiO<sub>2</sub> (green), Co@mSi<sub>x</sub>Al<sub>y</sub>O<sub>z</sub> (purple), Co@silicalite-1 (blue) and Co@HZSM5 (red).

promotes WGS directly or even indirectly by the reoxidation of small cobalt particles.<sup>[25]</sup> From *in situ* XAS results for Co@HZSM5 the presence of cobalt oxide after reduction and under reaction conditions is evident, which is known to be active for the WGS reaction.<sup>[36,37,68]</sup>

The methane selectivity increases with reaction temperature for Co@mSiO<sub>2</sub>, Co@mSi<sub>x</sub>Al<sub>y</sub>O<sub>z</sub> and Co@silicalite-1 as expected, exhibiting values comparable to literature for Co@mSiO<sub>2</sub> and Co@silicalite-1.<sup>[20,62]</sup> For Co@mSi<sub>x</sub>Al<sub>y</sub>O<sub>z</sub> Lapidus et al.<sup>[28]</sup> report values of 7–9% for Co/aluminosilicate materials at 190 °C, which corresponds well to our observations considering the temperature effect on selectivity. In contrast, Co@HZSM5 reaches a methane selectivity of 27% at 200 °C, already, which appears rather unaffected by temperature. One reason for this observation is the presence of cobalt oxide catalysing the WGS reaction and therefore leading to a locally higher H<sub>2</sub>/CO ratio favouring methane formation. The inverse relationship between methane selectivity and degree of reduction was also reported by Reuel

and Bartholomew.<sup>[68]</sup> The authors reported that the presence of unreduced cobalt oxides catalyse the WGS reaction and thus increase the H<sub>2</sub>/CO ratio of the reaction system, which would favour the hydrogenation of the adsorbed species leading to a higher CH<sub>4</sub> selectivity. A high methane selectivity for Co@HZSM5 at high temperature is frequently reported in literature, especially for Co/zeolites.<sup>[69]</sup> It is most probably caused by strong cobalt-zeolite interactions,<sup>[43,67]</sup> which could result in the stabilization of low coordinated Co sites and therefore in a higher methane selectivity as proposed by Sartipi et al.<sup>[67]</sup> This observation was also confirmed by Wang et al.,<sup>[43]</sup> who found the highest methane selectivity for the materials with the strongest cobalt-support interaction. Furthermore, hydrogenolysis of preferably heavier paraffins is taking place on group VIII metals like cobalt, which causes successive demethylation at the end of the hydrocarbon chain, forming methane and a heavier fragment.<sup>[41,42]</sup> The slight decrease in the methane selectivity of Co@HZSM5 at a reaction temperature of 250 °C

can be explained by the hydrocracking taking place, which increases the demand in  $H_2$  and therefore reduces the  $H_2$  partial pressure and thus methane selectivity.

For  $Co@mSiO_2$ ,  $Co@mSi_xAl_yO_z$  and  $Co@silicalite-1$  the  $C_2$ - $C_4$  selectivity is increasing with temperature, while the  $C_{5+}$  selectivity is decreasing, which is rather similar for all materials. This observation corresponds to the decreasing chain growth probability associated with higher temperatures.<sup>[32,70]</sup> For  $Co@HZSM5$ , in contrast, the  $C_2$ - $C_4$  selectivity reaches a plateau at  $260^\circ C$  and the  $C_{5+}$  selectivity is significantly reduced. Interestingly, the plateau in  $C_2$ - $C_4$  selectivity appears to be correlated to the high  $CO_2$  selectivity at the corresponding reaction temperature. Considering that the methane selectivity is constant and that hydrocracking of  $C_{5+}$  species should cause a higher amount of  $C_2$ - $C_4$  species, this observation is unexpected. However, it is reasonable considering the improved WGS activity provided by the presence of cobalt oxide species as discussed above. For a more detailed discussion of the product distribution for  $Co@mSiO_2$ ,  $Co@silicalite-1$ , and  $Co@HZSM5$  we refer to our recent work.<sup>[15]</sup>

## Conclusions

In this work, we applied a bottom-up approach to directly synthesize  $Co@HZSM5$  from a  $Co@mSi_xAl_yO_z$  precursor. For comparison,  $Co@silicalite-1$  was synthesized directly from a  $Co@mSiO_2$  material. The synthesized cobalt nanoparticles show comparable particle sizes of 30 nm for mesoporous and 25 nm for microporous materials, while the determined cobalt mass loadings between 7 and 9% are similar. XRD confirmed the successful conversion of the amorphous supporting shell materials to crystalline zeolite matrices. The presence of Al was confirmed via ICP. For  $Co@mSi_xAl_yO_z$  a Si/Al ratio of 109 was found, which indicates a high Al content, while a low acidity ( $0.12 \text{ mmol g}_{\text{cat}}^{-1}$ ) via  $NH_3$ -TPD was detected. In contrast, the  $Co@HZSM5$  material reveals a Si/Al ratio of 1851, but  $NH_3$ -TPD revealed an acidity of  $0.16 \text{ mmol g}_{\text{cat}}^{-1}$ , which is comparable to literature values.

*In situ* XAS experiments confirmed the presence of partly oxidized cobalt species in  $Co@HZSM5$  during the reaction, pointing to incomplete reduction under the protocol chosen here, while these species were associated with the high  $CO_2$  selectivity. As reasons for the high methane selectivity detected for  $Co@HZSM5$  hydrogenolysis and strong cobalt-support interactions are identified. The latter is also suggested to play a role in terms of methane selectivity of the amorphous aluminosilicate support.

Surprisingly, the FT results revealed the highest catalytic activity for  $Co@mSi_xAl_yO_z$ , even at high temperatures, while literature studies report low catalytic activity for these materials. In general, the catalytic activity of the materials with Al was found to be higher. This work highlights amorphous aluminosilicates as support materials for combined FT and HP synthesis giving a first insight into the catalytic activity and selectivities. Nevertheless, in future, the influence of the support material on

the  $C_{5+}$  products should be investigated to allow correlating structure and production of higher hydrocarbon products.

## Supporting information

In the supporting information we give additional information on:

- TEM images of the catalyst materials before and after FT reaction experiment
- Co particle size distribution before and after FT reaction experiment
- $H_2$ -TPR graph for each catalyst material
- Pore size distribution by  $N_2$  physisorption
- XRD patterns
- $NH_3$ -TPD experiment
- XANES analysis and linear combination fitting
- EXAFS results and fitting
- Cobalt time yields (CTYs) at all reaction temperatures
- Arrhenius plot and apparent activation energies

## Acknowledgements

The authors would like to thank Kang Cheng and Jogchum Oenema from ICC of Utrecht University for  $NH_3$ -TPD measurements. Dr. László Eifert from Helmholtz Institute Ulm is kindly thanked for the powder X-ray diffraction and the SEM measurements. In addition, we would like to thank the Institute for Beam Physics and Technology (IBPT) at Karlsruhe Institute of Technology (KIT) for the operation of the storage ring, the Karlsruhe Research Accelerator (KARA). We acknowledge Dr. Tim Prüßmann (INE/KIT) for his help and technical support during experiments at Cat-Act. Open Access funding enabled and organized by Projekt DEAL.

## Conflict of Interest

The authors declare no conflict of interest.

**Keywords:** aluminosilicate · cobalt catalysts · Fischer-Tropsch synthesis · X-ray absorption spectroscopy · zeolite

- [1] C. Le Quéré, R. Moriarty, R. M. Andrew, J. G. Canadell, S. Sitch, J. I. Korsbakken, P. Friedlingstein, G. P. Peters, R. J. Andres, T. A. Boden, R. A. Houghton, J. I. House, R. F. Keeling, P. Tans, A. Arneeth, D. C. E. Bakker, L. Barbero, L. Bopp, J. Chang, F. Chevallier, L. P. Chini, P. Ciais, M. Fader, R. A. Feely, T. Gkritzalis, I. Harris, J. Hauck, T. Ilyina, A. K. Jain, E. Kato, V. Kitidis, K. Klein Goldewijk, C. Koven, P. Landschützer, S. K. Lausset, N. Lefèvre, A. Lenton, I. D. Lima, N. Metz, F. Millero, D. R. Munro, A. Murata, J. E. M. S. Nabel, S. Nakaoka, Y. Nojiri, K. O'Brien, A. Olsen, T. Ono, F. F. Pérez, B. Pfeil, D. Pierrot, B. Poulter, G. Rehder, C. Rödenbeck, S. Saito, U. Schuster, J. Schwinger, R. Séférian, T. Steinhoff, B. D. Stocker, A. J. Sutton, T. Takahashi, B. Tilbrook, I. T. van der Laan-Luijckx, G. R. van der Werf, S. van Heuven, D. Vandemark, N. Viovy, A. Wiltshire, S. Zaehle, N. Zeng, *Earth Syst. Sci. Data* **2015**, *7*, 349–396.
- [2] United Nations, "The Paris Agreement", to be found under [https://unfccc.int/files/meetings/paris\\_nov\\_2015/application/pdf/paris\\_agreement\\_english\\_.pdf](https://unfccc.int/files/meetings/paris_nov_2015/application/pdf/paris_agreement_english_.pdf), 2015.

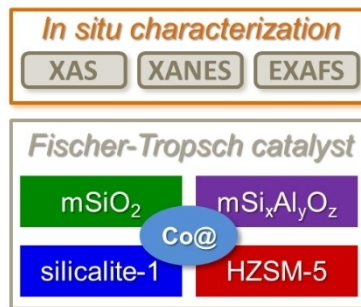
- [3] Z. He, M. Cui, Q. Qian, J. Zhang, H. Liu, B. Han, *Proc. Natl. Acad. Sci. USA* **2019**, *116*, 12654–12659.
- [4] S. Falcinelli, *Catal. Today* **2020**, *348*, 95–101.
- [5] M. N. Anwar, A. Fayyaz, N. F. Sohail, M. F. Khokhar, M. Baqar, A. Yasar, K. Rasool, A. Nazir, M. U. F. Raja, M. Rehan, M. Aghbashlo, M. Tabatabaei, A. S. Nzami, *J. Environ. Manag.* **2020**, *260*, 110059.
- [6] H. Kirsch, N. Lochmahr, C. Staudt, P. Pfeifer, R. Dittmeyer, *Chem. Eng. J.* **2020**, *393*, 124553.
- [7] M. Loewert, P. Pfeifer, *ChemEngineering* **2020**, *4*, 21.
- [8] E. Bargiacchi, M. Antonelli, U. Desideri, *Energy* **2019**, *183*, 1253–1265.
- [9] R. Güttel, T. Turek, *Energy Technol.* **2016**, *4*, 44–54.
- [10] C. Sun, P. Pfeifer, R. Dittmeyer, *Chem. Eng. J.* **2017**, *326*, 37–46.
- [11] A. Martinez, J. Rollan, M. Arribas, H. Cerqueira, A. Costa, E. F. S. Aguiar, *J. Catal.* **2007**, *249*, 162–173.
- [12] C. Zhu, G. M. Bollas, *Appl. Catal. B* **2018**, *235*, 92–102.
- [13] J. H. Lee, W. Bonte, S. Corthals, F. Krumeich, M. Ruitenbeek, J. A. van Bokhoven, *Ind. Eng. Chem. Res.* **2019**, *58*, 5140–5145.
- [14] W. Li, Y. He, H. Li, D. Shen, C. Xing, R. Yang, *Catal. Commun.* **2017**, *98*, 98–101.
- [15] A. Straß-Eifert, L. I. Wal, C. Hernández Mejía, L. J. Weber, H. Yoshida, J. Zečević, K. P. Jong, R. Güttel, *ChemCatChem* **2021**, *13*, 2726–2742.
- [16] K. Pabst, B. Kraushaar-Czarnetzki, G. Schaub, *Ind. Eng. Chem. Res.* **2013**, *52*, 8988–8995.
- [17] A. Carvalho, M. Marinova, N. Batalha, N. R. Marcilio, A. Y. Khodakov, V. V. Ordonsky, *Catal. Sci. Technol.* **2017**, *7*, 5019–5027.
- [18] S. Sartipi, K. Parashar, M. Makkee, J. Gascon, F. Kapteijn, *Catal. Sci. Technol.* **2013**, *3*, 572–575.
- [19] C. Flores, N. Batalha, N. R. Marcilio, V. V. Ordonsky, A. Y. Khodakov, *ChemCatChem* **2019**, *11*, 568–574.
- [20] S.-H. Kang, J.-H. Ryu, J.-H. Kim, P. S. Sai Prasad, J. W. Bae, J.-Y. Cheon, K.-W. Jun, *Catal. Lett.* **2011**, *141*, 1464–1471.
- [21] M. Javed, S. Cheng, G. Zhang, C. C. Amoo, J. Wang, P. Lu, C. Lu, C. Xing, J. Sun, N. Tsubaki, *Chin. J. Catal.* **2020**, *41*, 604–612.
- [22] C. Liu, Y. Chen, Y. Zhao, S. Lyu, L. Wei, X. Li, Y. Zhang, J. Li, *Fuel* **2020**, *263*, 116619.
- [23] X. Li, J. He, M. Meng, Y. Yoneyama, N. Tsubaki, *J. Catal.* **2009**, *265*, 26–34.
- [24] M. Javed, S. Cheng, G. Zhang, P. Dai, Y. Cao, C. Lu, R. Yang, C. Xing, S. Shan, *Fuel* **2018**, *215*, 226–231.
- [25] J. Liu, D. Wang, J.-F. Chen, Y. Zhang, *Int. J. Hydrogen Energy* **2016**, *41*, 21965–21978.
- [26] D. X. Martinez-Vargas, L. Sandoval-Rangel, O. Campuzano-Calderon, M. Romero-Flores, F. J. Lozano, K. D. P. Nigam, A. Mendoza, A. Montesinos-Castellanos, *Ind. Eng. Chem. Res.* **2019**, *58*, 15872–15901.
- [27] J. Hwang, G. Kwak, Y.-J. Lee, Y. T. Kim, I. Jeong, S. Kim, K.-W. Jun, K.-S. Ha, J. Lee, *J. Mater. Chem. A* **2015**, *3*, 23725–23731.
- [28] A. L. Lapidus, V. A. Pavlova, N. K. Chin, O. L. Eliseyev, V. V. Gushchin, P. E. Davydov, *Pet. Chem.* **2009**, *49*, 301–305.
- [29] Y. Wang, Y. Jiang, J. Huang, H. Wang, Z. Li, J. Wu, *RSC Adv.* **2016**, *6*, 107498–107506.
- [30] Y. Wang, X. Li, H. Ma, H. Zhang, Y. Jiang, H. Wang, Z. Li, J. Wu, *React. Kinet. Mech. Catal.* **2017**, *120*, 775–790.
- [31] Q. Lin, Q. Zhang, G. Yang, Q. Chen, J. Li, Q. Wei, Y. Tan, H. Wan, N. Tsubaki, *J. Catal.* **2016**, *344*, 378–388.
- [32] D. Vervloet, F. Kapteijn, J. Nijenhuis, J. R. van Ommen, *Catal. Sci. Technol.* **2012**, *2*, 1221.
- [33] M. Lualdi, S. Lögdberg, F. Regali, M. Boutonnet, S. Järås, *Top. Catal.* **2011**, *54*, 977–985.
- [34] R. B. Anderson, K. W. Hall, A. Krieg, B. Seligman, *J. Catal.* **1949**, *92*, 367–387.
- [35] A. Y. Khodakov, A. Griboval-Constant, R. Bechara, V. L. Zholobenko, *J. Catal.* **2002**, *206*, 230–241.
- [36] A. Bao, K. Liew, J. Li, *J. Mol. Catal. A* **2009**, *304*, 47–51.
- [37] K. S. Park, K. Saravanan, S.-J. Park, Y.-J. Lee, K.-W. Jeon, J. W. Bae, *Catal. Sci. Technol.* **2017**, *7*, 4079–4091.
- [38] G. L. Bezemer, J. H. Bitter, H. P. C. E. Kuipers, H. Oosterbeek, J. E. Holewijn, X. Xu, F. Kapteijn, A. J. van Dillen, K. P. de Jong, *J. Am. Chem. Soc.* **2006**, *128*, 3956–3964.
- [39] X. Fang, B. Liu, K. Cao, P. Yang, Q. Zhao, F. Jiang, Y. Xu, R. Chen, X. Liu, *ACS Catal.* **2020**, *10*, 2799–2816.
- [40] L. Fu, C. H. Bartholomew, *J. Catal.* **1985**, *92*, 376–387.
- [41] X. Peng, K. Cheng, J. Kang, B. Gu, X. Yu, Q. Zhang, Y. Wang, *Angew. Chem. Int. Ed.* **2015**, *54*, 4553–4556; *Angew. Chem.* **2015**, *127*, 4636–4639.
- [42] J. H. Sinfelt, *Adv. Catal.* **1973**, *23*, 91–119.
- [43] Y. Wang, J. Yu, J. Qiao, Y. Sun, W. Jin, H. Zhang, J. Ma, *J. Energy Inst.* **2020**, *93*, 1187–1194.
- [44] J. Ilsemann, A. Straß-Eifert, J. Friedland, L. Kiewidt, J. Thöming, M. Bäumer, R. Güttel, *ChemCatChem* **2019**, *11*, 4884–4893.
- [45] N. Kruse, A. G. Machoke, W. Schwieger, R. Güttel, *ChemCatChem* **2015**, *7*, 1018–1022.
- [46] J. Schindelin, I. Arganda-Carreras, E. Frise, V. Kaynig, M. Longair, T. Pietzsch, S. Preibisch, C. Rueden, S. Saalfeld, B. Schmid, J.-Y. Tinevez, D. J. White, V. Hartenstein, K. Eliceiri, P. Tomancak, A. Cardona, *Nat. Methods* **2012**, *9*, 676–682.
- [47] S. Sartipi, J. E. van Dijk, J. Gascon, F. Kapteijn, *Appl. Catal. A* **2013**, *456*, 11–22.
- [48] A. Zimina, K. Dardenne, M. A. Denecke, D. E. Doronkin, E. Huttel, H. Lichtenberg, S. Mangold, T. Pruessmann, J. Rothe, T. Spangenberg, R. Steininger, T. Vitova, H. Geckeis, J.-D. Grunwaldt, *Rev. Sci. Instrum.* **2017**, *88*, 113113.
- [49] J.-D. Grunwaldt, N. van Vegten, A. Baiker, *Chem. Commun.* **2007**, 4635–4637.
- [50] B. Ravel, M. Newville, *J. Synchrotron Radiat.* **2005**, *12*, 537–541.
- [51] J. Knochen, R. Güttel, C. Knobloch, T. Turek, *Chem. Eng. Process.* **2010**, *49*, 958–964.
- [52] M. Wolf, E. K. Gibson, E. J. Olivier, J. H. Neethling, C. R. A. Catlow, N. Fischer, M. Claeys, *Catal. Today* **2020**, *342*, 71–78.
- [53] N. V. Beznis, B. M. Weckhuysen, J. H. Bitter, *Catal. Lett.* **2010**, *136*, 52–56.
- [54] J. M. Fedeyko, H. Ego-Fox, D. W. Fickel, D. G. Vlachos, R. F. Lobo, *Langmuir* **2007**, *23*, 4532–4540.
- [55] N.-Y. Topsoe, K. Pedersen, E. G. Derouane, *J. Catal.* **1981**, *70*, 41–52.
- [56] C. V. Hidalgo, H. Itho, T. Hattori, M. Niwa, Y. Murakami, *J. Catal.* **1984**, *85*, 362–369.
- [57] C. Jacobsen, C. Madsen, T. Janssens, H. J. Jakobsen, J. Skibsted, *Microporous Mesoporous Mater.* **2000**, *39*, 393–401.
- [58] N. V. Beznis, A. N. van Laak, B. M. Weckhuysen, J. H. Bitter, *Microporous Mesoporous Mater.* **2011**, *138*, 176–183.
- [59] V. E. Henrich, P. A. Cox, *The Surface Science of Metal Oxides*, Cambridge University Press, Cambridge, **1996**.
- [60] B. Ernst, A. Bensaddik, L. Hilaire, P. Chaumette, A. Kiennemann, *Catal. Today* **1998**, *39*, 329–341.
- [61] A. Straß-Eifert, T. L. Sheppard, C. D. Damsgaard, J.-D. Grunwaldt, R. Güttel, *ChemCatChem* **2021**, *13*, 718–729.
- [62] R. Xie, D. Li, B. Hou, J. Wang, L. Jia, Y. Sun, *Catal. Commun.* **2011**, *12*, 380–383.
- [63] B. Zeng, B. Hou, L. Jia, J. Wang, C. Chen, D. Li, Y. Sun, *Catal. Sci. Technol.* **2013**, *3*, 3250.
- [64] N. E. Tsakoumis, M. Rønning, Ø. Borg, E. Rytter, A. Holmen, *Catal. Today* **2010**, *154*, 162–182.
- [65] M. Rahmati, M.-S. Safdari, T. H. Fletcher, M. D. Argyle, C. H. Bartholomew, *Chem. Rev.* **2020**, *120*, 4455–4533.
- [66] C. H. Bartholomew, *Appl. Catal. A* **2001**, *212*, 17–60.
- [67] S. Sartipi, K. Parashar, M. J. Valero-Romero, V. P. Santos, B. van der Linden, M. Makkee, F. Kapteijn, J. Gascon, *J. Catal.* **2013**, *305*, 179–190.
- [68] R. C. Reuel, C. H. Bartholomew, *J. Catal.* **1984**, *85*, 78–88.
- [69] C. Flores, N. Batalha, V. V. Ordonsky, V. L. Zholobenko, W. Baaziz, N. R. Marcilio, A. Y. Khodakov, *ChemCatChem* **2018**, *10*, 2291–2299.
- [70] H. Becker, R. Güttel, T. Turek, *Catal. Sci. Technol.* **2019**, *9*, 2180–2195.

Manuscript received: July 13, 2021  
Revised manuscript received: September 6, 2021  
Accepted manuscript online: October 4, 2021  
Version of record online: ■■■, ■■■■

## FULL PAPERS

---

**Fischer-Tropsch synthesis:** Four types of bi-functional catalysts with cobalt nanoparticles supported on meso- or microporous silicates or aluminosilicates are investigated regarding the obtained CO<sub>2</sub> and CH<sub>4</sub> selectivity under low-temperature Fischer-Tropsch reaction conditions. *In situ* x-ray absorption spectroscopy results under industrially relevant conditions reveal that strong cobalt-support interactions and oxidized cobalt species are the main factors determining the selectivity depending on the specific support material used.



Dr. A. Straß-Eifert, Dr. T. L. Sheppard,  
Dr. H. Becker, Dr. J. Friedland, Dr. A.  
Zimina, Prof. J.-D. Grunwaldt, Prof. R.  
Güttel\*

1 – 13

**Cobalt-based Nanoreactors in  
Combined Fischer-Tropsch  
Synthesis and Hydroprocessing:  
Effects on Methane and CO<sub>2</sub> Selec-  
tivity**

